

Article

New $\text{BaTi}_{0.96}\text{Cu}_{0.02}\text{X}_{0.02}\text{O}_3$ ($\text{X} = \text{V}, \text{Nb}$) Photocatalysts for Dyes Effluent Remediation: Broad Visible Light Response

Ghayah M. Alsulaim

Department of Chemistry, College of Science, King Faisal University, Al-Ahsa 31982, Saudi Arabia; galsaleem@kfu.edu.sa or g.m.alsulaim@gmail.com

Abstract: The problem of industrial dyes depollution has pushed the scientific research community to identify novel photocatalysts with high performance. Herein, new photocatalysts composed of BaTiO_3 , $\text{BaTi}_{0.96}\text{Cu}_{0.04}\text{O}_3$, $\text{BaTi}_{0.96}\text{Cu}_{0.02}\text{V}_{0.02}\text{O}_3$ and $\text{BaTi}_{0.96}\text{Cu}_{0.02}\text{Nb}_{0.02}\text{O}_3$ powders were prepared by solid-state reaction. The structural analysis of the samples confirmed the formation of the BaTiO_3 structure. The splitting of (002) and (200) planes verified the formation of the tetragonal phase. The XRD peaks shifted, and the unit cell volume expansion verified the substitution of the Ti^{4+} site by Cu^{2+} , V^{4+} and Nb^{5+} ions. The morphological measurements showed that the addition of (Cu, V) and (Cu, Nb) ions changes the particles' morphology of BaTiO_3 , reducing its grains size. After the incorporation of (Cu, V) and (Cu, Nb) ions, the band gap of BaTiO_3 was reduced from 3.2 to 2.84 and 2.72 eV, respectively. The modification of BaTiO_3 by (Cu, Nb) ions induced superior photocatalytic properties for methyl green and methyl orange with degradation efficiencies of 97% and 94% during 60 and 90 min under sunlight irradiation, respectively. The total organic carbon results indicated that the $\text{BaTi}_{0.96}\text{Cu}_{0.02}\text{Nb}_{0.02}\text{O}_3$ catalyst has a high mineralization efficiency. In addition, it possesses a high stability during three cycles. The high photodegradation efficiency of $\text{Bi}_{0.96}\text{La}_{0.02}\text{Gd}_{0.02}\text{FeO}_3$ was related to the wide-ranging visible light absorption.

Keywords: perovskite BaTiO_3 semiconductor; new visible light photocatalysts; environmental and water pollution; organic dyes; xenon lamp and solar energy



Citation: Alsulaim, G.M. New $\text{BaTi}_{0.96}\text{Cu}_{0.02}\text{X}_{0.02}\text{O}_3$ ($\text{X} = \text{V}, \text{Nb}$) Photocatalysts for Dyes Effluent Remediation: Broad Visible Light Response. *Catalysts* **2023**, *13*, 1365. <https://doi.org/10.3390/catal13101365>

Academic Editor: Bo Weng

Received: 28 August 2023

Revised: 27 September 2023

Accepted: 10 October 2023

Published: 12 October 2023



Copyright: © 2023 by the author. Licensee MDPI, Basel, Switzerland. This article is an open access article distributed under the terms and conditions of the Creative Commons Attribution (CC BY) license (<https://creativecommons.org/licenses/by/4.0/>).

1. Introduction

Human, animals, plants and aquatic life need a clean environment and pure water supply. Many industrial activities discharge large quantities of organic dyes pollutants into water resources [1,2]. These dyes are non-biodegradable, very hazardous and carcinogenic and can cause harm to all organisms even at low concentrations [3]. The paper, textile, paint, nylon, silk, cosmetics, plastics and leather industries are the main sources of dyes waste with nearly 200,000 tons of these organic dyes being dumped into water sources annually [4]. Photocatalysis is a potential green method to solve the dyes pollution problem through using a light energy source (UV or visible light) and active photocatalysts [1–5]. Hydrogen production by the photocatalytic water-splitting technique has been considered as a promising methodology to produce renewable energy [6]. In the photocatalysis process, a suitable light energy was used to activate the particles of the catalysts to produce charge carriers (electron–hole pairs) which later yielded very reactive radicals such as $\text{O}_2^{\bullet-}$ and $\cdot\text{OH}$ species [4,7]. These reactive radicals can attack the organic dyes molecules and mineralize them to non-harmful products (CO_2 and H_2O) [4–8]. The dyes depollution issue pushes the scientific research community toward the synthesis of low-cost, stable, non-toxic and highly efficient photocatalysts [9–11]. Numerous photocatalytic studies have been carried out on metal oxides, sulfides and perovskite materials like ZnO [12], TiO_2 [13], CuS [14], ZnS [15], Fe_2O_3 [16], WO_3 [5], $\text{g-C}_3\text{N}_4$ [17] and BaTiO_3 [18]. BaTiO_3 -based materials were candidates as promising catalysts for the photodegradation of organic contaminants and bacterial disinfection in wastewater [19,20]. The perovskite BaTiO_3 semiconductor has a wide band

gap energy varying from 3.2 to 3.4 eV [21]. Engineering the band gap energy of the BaTiO₃ material to absorb the visible light spectrum is practically useful for the photocatalytic applications [22]. Bhat et al. [22] studied the effect of Rh doping on the photocatalytic activity of BaTiO₃ material for the degradation of methylene blue dye (10 mg/L) under visible light irradiation. They found that 0.5 mol% Rh doping enhances the photocatalytic activity of BaTiO₃ toward methylene blue dye with a photodegradation efficiency of 96% during 120 min of irradiation. The Mn-doped BaTiO₃ nanotube as a photocatalyst exhibited improved visible light photocatalytic activity for methylene blue dye over 300 min [23]. The photodegradation properties of the 5% Ag-doped BaTiO₃ catalyst was investigated for 20 mg/L rhodamine B dye under visible light irradiation [24]. After 105 min, this catalyst has shown a visible light photodegradation efficiency of 79%. Cu-doped BaTiO₃ revealed photocatalytic activities of 98.2% for 10 mg/L methylene blue dye during 120 min and 99.4% for 10 mg/L rose Bengal dye within 45 min [18]. Amaechi et al. [25] showed that the 2% Fe³⁺-doped BaTiO₃ nanocatalyst has a sunlight photodegradation efficiency of 75% for 20 mg/L methyl orange. Based on our knowledge, there is no available study on the influence of (Cu, V) and (Cu, Nb) codoping on the photodegradation properties of BaTiO₃ for methyl green and methyl orange pollutants under natural sunlight and Xenon lamp photoreactor irradiation. The Cu, V and Nb elements as dopants have the ability to engineer the visible light response of BaTiO₃. These dopants possess variable oxidation states which can inhibit the recombination of the charge carriers (electron–hole pairs) through acting as trap centers. Herein, new catalysts composed of BaTiO₃, BaTi_{0.96}Cu_{0.04}O₃, BaTi_{0.96}Cu_{0.02}V_{0.02}O₃ and BaTi_{0.96}Cu_{0.02}Nb_{0.02}O₃ powders were prepared by the solid-state reaction method. The structural, morphological and optical properties of the synthesized samples were investigated and discussed. In addition, the photocatalytic properties of BaTiO₃, BaTi_{0.96}Cu_{0.04}O₃, BaTi_{0.96}Cu_{0.02}V_{0.02}O₃ and BaTi_{0.96}Cu_{0.02}Nb_{0.02}O₃ powders for the degradation of methyl green and methyl orange dyes were measured under natural sunlight and Xenon lamp photoreactor irradiation. The obtained results indicated that the BaTi_{0.96}Cu_{0.02}Nb_{0.02}O₃ catalyst possesses high sunlight photodegradation and mineralization efficiencies for 20 mg/L methyl green and methyl orange dyes after 60 and 90 min, respectively. In addition, the BaTi_{0.96}Cu_{0.02}Nb_{0.02}O₃ catalyst exhibits a high photodegradation stability for both dyes during three cycles under sunlight.

2. Results and Discussion

2.1. X-ray Diffraction (XRD) Analysis

Figure 1 demonstrates the X-ray diffraction patterns of the pure BaTiO₃, BaTi_{0.96}Cu_{0.04}O₃, BaTi_{0.96}Cu_{0.02}V_{0.02}O₃ and BaTi_{0.96}Cu_{0.02}Nb_{0.02}O₃ powders within a 2-theta angle of 10–80°. The pure BaTiO₃ sample exhibits nine X-ray diffraction peaks at 2θ values equal to 22.401°, 31.722°, 39.101°, 44.69°, 45.421°, 51.112°, 56.299°, 66.031° and 75.102°, which were indexed to (100), (110), (111), (002), (200), (201), (211), (220) and (310) crystallographic planes of a tetragonal BaTiO₃ structure (standard JCPDS, card file No. 05-0626, P4/mmm space group). The compositions of BaTi_{0.96}Cu_{0.04}O₃, BaTi_{0.96}Cu_{0.02}V_{0.02}O₃ and BaTi_{0.96}Cu_{0.02}Nb_{0.02}O₃ powders display analogous X-ray diffraction peaks to that of the pure BaTiO₃ sample, indicating also the formation of a tetragonal BaTiO₃ structure. For all samples, the splitting of (002) and (200) planes within 2θ = 44–46° (inset Figure 1) verifies the formation of the tetragonal phase and ruled out the existence of a cubic BaTiO₃ phase (both planes combine in one peak in case of a cubic BaTiO₃ structure) [26]. As presented in Table 1, the ratio of (c/a) supported the formation of the tetragonal phase for all samples. The absence of any impurities can be deduced from the non-existence of any other X-ray diffraction peaks in these patterns. The X-ray diffraction peaks of all samples have high intensities, which reflect the good crystallinity. The influence of the incorporation of Cu, (Cu, V) and (Cu, Nb) ions on the 2θ angle of the (110) and (111) planes of the BaTiO₃ structure is illustrated in Figure 2. It can be seen that both planes of BaTiO₃ were shifted to a lower 2θ angle owing to doping and dual doping by Cu, (Cu, V) and (Cu, Nb) ions. The ionic radius of the Ba²⁺ site is 1.61 Å in the XII coordination, while that of the Ti⁴⁺ site is 0.605 Å in the VI coordination.

The ionic radii of Cu^{2+} , V^{4+} and Nb^{5+} ions in the VI coordination are 0.73 Å, 0.58 Å and 0.64 Å, respectively. The detected shifts to a lower 2θ angle suggested the replacement of the Ti^{4+} site (0.605 Å) by Cu^{2+} , V^{4+} and Nb^{5+} ions of larger or close ionic radii. As shown in Figure 3 and Table 1, the calculations of the unit cell volume illustrate the expansion of the lattice parameters and unit cell volume of pure BaTiO_3 after the incorporation of Cu^{2+} , V^{4+} and Nb^{5+} ions, confirming the effective substitution process. These increases in the unit cell volume of BaTiO_3 can be assigned to the larger ionic radii, especially Cu^{2+} and Nb^{5+} ions compared to Ti^{4+} site (0.605 Å). The average crystallite size of the BaTiO_3 , $\text{BaTi}_{0.96}\text{Cu}_{0.04}\text{O}_3$, $\text{BaTi}_{0.96}\text{Cu}_{0.02}\text{V}_{0.02}\text{O}_3$ and $\text{BaTi}_{0.96}\text{Cu}_{0.02}\text{Nb}_{0.02}\text{O}_3$ samples were estimated by using the Williamson Hall equation as shown below [27]:

$$\beta \cos \theta = (K\lambda/D) + 4\epsilon \sin \theta \quad (1)$$

where β represents the full width at half maximum (radian), θ is the angle of the peaks in radians, K is a constant (0.9), λ is the wavelength of the X-ray radiation, D is the crystallite size and ϵ is the microstrain. By plotting $4\sin \theta$ (X-axis) with $\beta \cos \theta$ (Y-axis), the average crystallite size can be estimated from the intercept of the fitting line, while the microstrain can be found from the slope. As illustrated in Figure 4, the average crystallite size of pure BaTiO_3 , $\text{BaTi}_{0.96}\text{Cu}_{0.04}\text{O}_3$, $\text{BaTi}_{0.96}\text{Cu}_{0.02}\text{V}_{0.02}\text{O}_3$ and $\text{BaTi}_{0.96}\text{Cu}_{0.02}\text{Nb}_{0.02}\text{O}_3$ powders were estimated to be 72, 62, 58 and 56 nm, respectively.

Table 1. Crystallite size D , lattice parameters (a , b , c), c/a ratio, unit cell volume (V) of pure BaTiO_3 , $\text{BaTi}_{0.96}\text{Cu}_{0.04}\text{O}_3$, $\text{BaTi}_{0.96}\text{Cu}_{0.02}\text{V}_{0.02}\text{O}_3$ and $\text{BaTi}_{0.96}\text{Cu}_{0.02}\text{Nb}_{0.02}\text{O}_3$ samples.

Samples	D (nm)	a Å	b Å	c Å	c/a	V Å ³
BaTiO_3	71	3.9987	3.9987	4.0111	1.0031	64.1359
$\text{BaTi}_{0.96}\text{Cu}_{0.04}\text{O}_3$	61	4.0002	4.0002	4.0174	1.0038	64.2861
$\text{BaTi}_{0.96}\text{Cu}_{0.02}\text{V}_{0.02}\text{O}_3$	58	4.0008	4.0008	4.0143	1.0033	64.2535
$\text{BaTi}_{0.96}\text{Cu}_{0.02}\text{Nb}_{0.02}\text{O}_3$	56	4.0007	4.0007	4.0150	1.0035	64.2639

2.2. Scanning Electron Microscope (SEM) Analysis

The scanning electron microscope (SEM) images of the synthesized pure BaTiO_3 , $\text{BaTi}_{0.96}\text{Cu}_{0.04}\text{O}_3$, $\text{BaTi}_{0.96}\text{Cu}_{0.02}\text{V}_{0.02}\text{O}_3$ and $\text{BaTi}_{0.96}\text{Cu}_{0.02}\text{Nb}_{0.02}\text{O}_3$ powders and the effect of dopants on morphology are shown in Figure 5. The SEM image of the pure BaTiO_3 sample reveals the synthesis of coagulated large grains, which possess an asymmetrical shape with an irregular edge. The Cu doping into the BaTiO_3 lattice somewhat reduces the size of the grains, but they are still coagulated together. In contrast, the addition of the dual dopants of (Cu, V) and (Cu, Nb) ions powerfully changes the morphology of BaTiO_3 and leads to the formation of uniform semispherical particles with reduced grain size. These results point out that (Cu, V) and (Cu, Nb) ions have a strong restriction effect on the growth of the BaTiO_3 grains during the calcination process at high temperature. The energy-dispersive X-ray (EDX) investigation was carried out to analyze the elemental composition of the synthesized samples, as demonstrated in Figure 6. The patterns of the energy-dispersive X-ray spectra of $\text{BaTi}_{0.96}\text{Cu}_{0.02}\text{V}_{0.02}\text{O}_3$ and $\text{BaTi}_{0.96}\text{Cu}_{0.02}\text{Nb}_{0.02}\text{O}_3$ powders verify the presence of Ba, Ti, O, Cu, V and Nb elements and ruled out the existence of any other impurity elements. The wt. % of the dopants elements, including Cu, V and Nb ions, is close with the added values during the synthesis process.

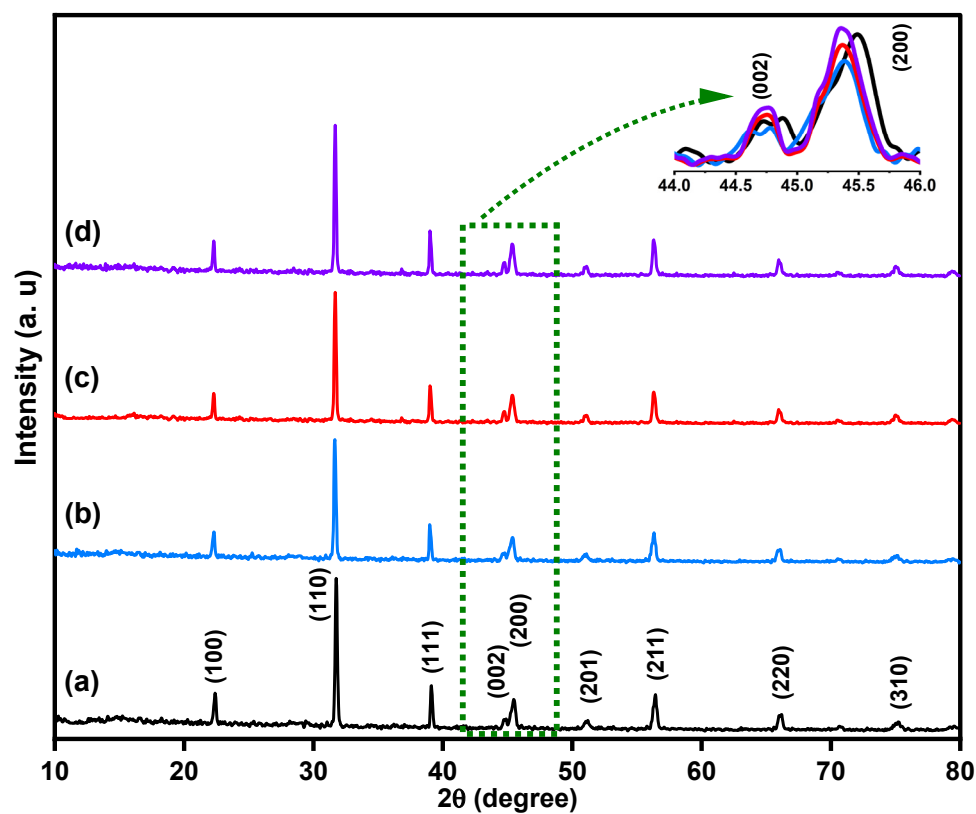


Figure 1. Crystal structure based on X-ray diffraction analysis of (a) BaTiO_3 , (b) $\text{BaTi}_{0.96}\text{Cu}_{0.04}\text{O}_3$, (c) $\text{BaTi}_{0.96}\text{Cu}_{0.02}\text{V}_{0.02}\text{O}_3$ and (d) $\text{BaTi}_{0.96}\text{Cu}_{0.02}\text{Nb}_{0.02}\text{O}_3$ samples.

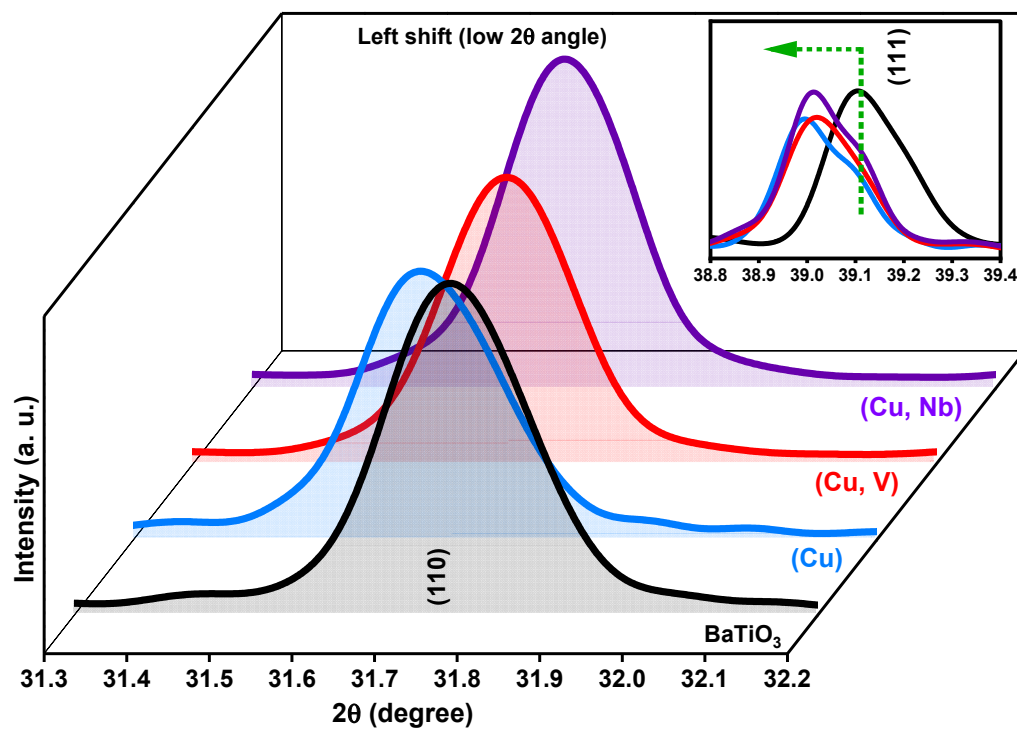


Figure 2. Impact of incorporation of Cu, (Cu, V) and (Cu, Nb) ions on 2θ angle of (110) and (111) crystallographic planes of BaTiO_3 structure.

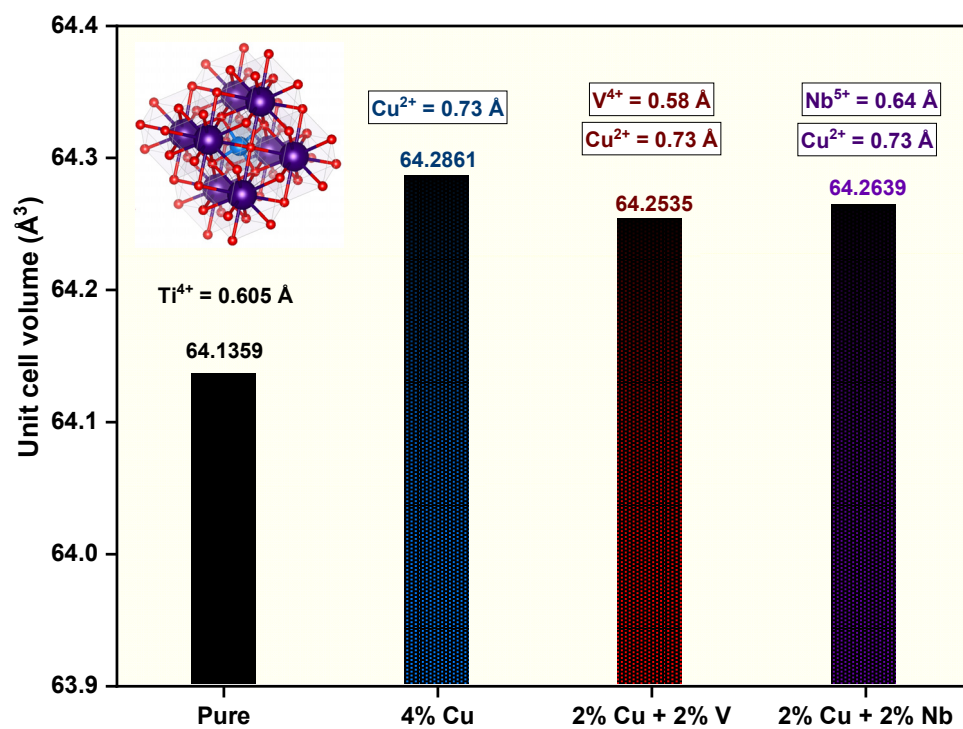


Figure 3. Impact of incorporation of Cu, (Cu, V) and (Cu, Nb) ions on unit cell volume of pure BaTiO₃ sample.

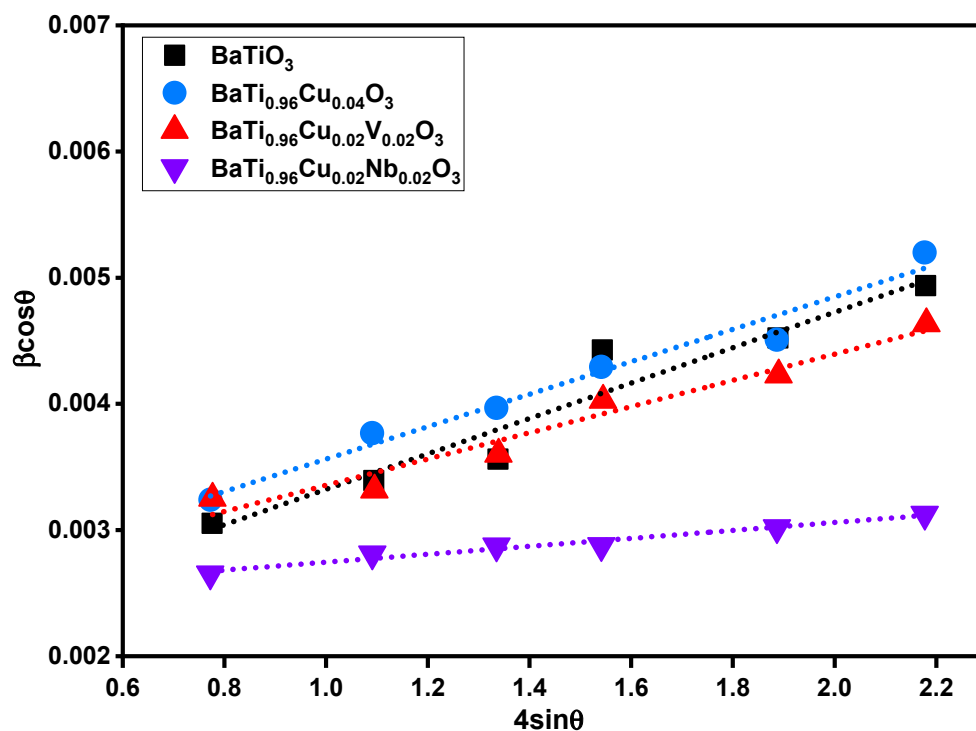


Figure 4. Williamson–Hall plots of BaTiO₃, BaTi_{0.96}Cu_{0.04}O₃, BaTi_{0.96}Cu_{0.02}V_{0.02}O₃ and BaTi_{0.96}Cu_{0.02}Nb_{0.02}O₃ samples for crystallite size estimation.

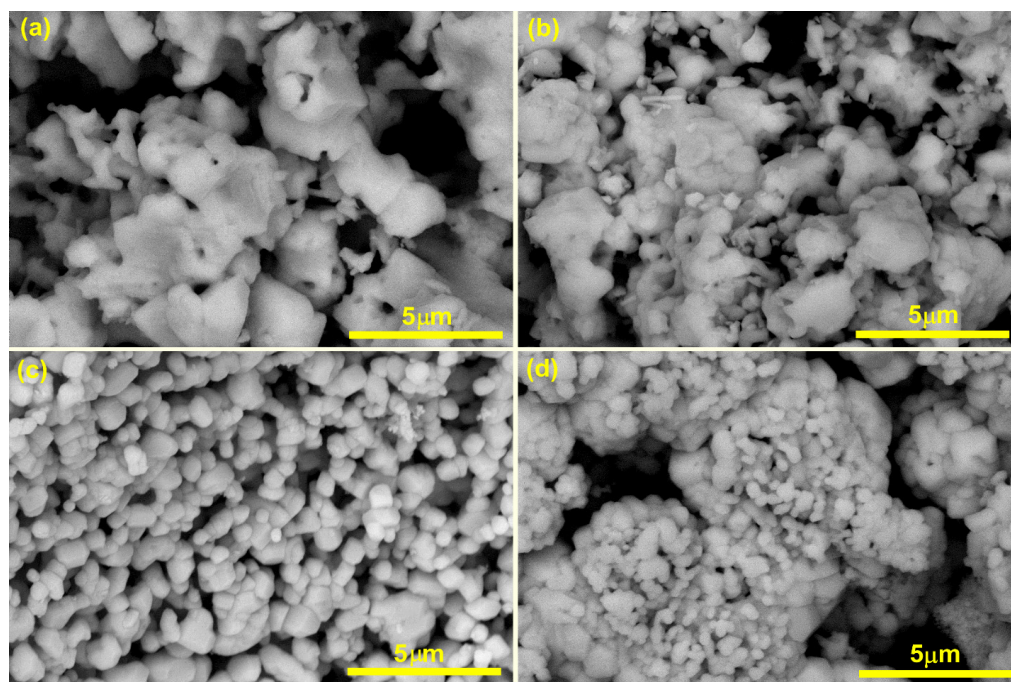


Figure 5. Scanning electron microscope images of (a) BaTiO_3 , (b) $\text{BaTi}_{0.96}\text{Cu}_{0.04}\text{O}_3$, (c) $\text{BaTi}_{0.96}\text{Cu}_{0.02}\text{V}_{0.02}\text{O}_3$ and (d) $\text{BaTi}_{0.96}\text{Cu}_{0.02}\text{Nb}_{0.02}\text{O}_3$ powders.

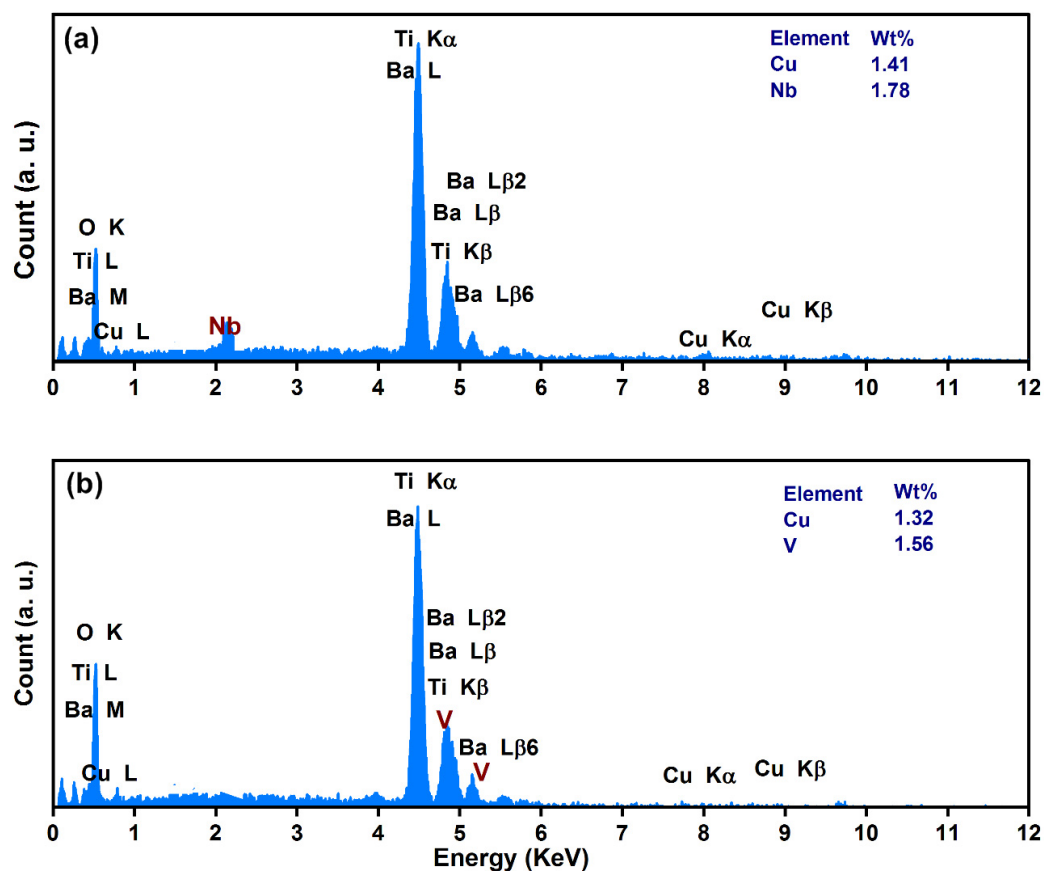


Figure 6. Energy-dispersive X-ray (EDX) spectra of (a) $\text{BaTi}_{0.96}\text{Cu}_{0.02}\text{V}_{0.02}\text{O}_3$ and (b) $\text{BaTi}_{0.96}\text{Cu}_{0.02}\text{Nb}_{0.02}\text{O}_3$ powders.

2.3. Optical Properties and Band Gap Energy

The effective photocatalysis process is strongly related to the optical properties and the band gap energy of the used catalysts. The diffuse reflectance (DR) analysis was carried out to investigate the optical properties of the pure BaTiO_3 , $\text{BaTi}_{0.96}\text{Cu}_{0.04}\text{O}_3$, $\text{BaTi}_{0.96}\text{Cu}_{0.02}\text{V}_{0.02}\text{O}_3$ and $\text{BaTi}_{0.96}\text{Cu}_{0.02}\text{Nb}_{0.02}\text{O}_3$ catalysts within a wavelength of 200–2400 nm, as shown in Figure 7. The reflectance spectrum (%) of the pure BaTiO_3 catalyst has a high intensity (80–90%) within 400–2400 nm, while below 400 nm, the reflectance (%) intensely decreased in a sharp manner (absorption edge), which matches with the band gap energy absorption of the pure BaTiO_3 structure. The addition of Cu^{2+} , V^{4+} and Nb^{5+} ions strongly reduces the intensity of the reflectance and also shifts the absorption edge to a longer wavelength (low energy). The diffuse reflectance spectra display that Cu, (Cu, V) and (Cu, Nb) ions enhance the visible light absorption capacity of the BaTiO_3 catalyst. The Tauc and Kubelka–Munk equations were used to estimate the band gap energy of pure BaTiO_3 , $\text{BaTi}_{0.96}\text{Cu}_{0.04}\text{O}_3$, $\text{BaTi}_{0.96}\text{Cu}_{0.02}\text{V}_{0.02}\text{O}_3$ and $\text{BaTi}_{0.96}\text{Cu}_{0.02}\text{Nb}_{0.02}\text{O}_3$ catalysts as displayed below [28]:

$$\alpha = A(h\nu - E_g)^n/h\nu \quad (2)$$

$$F(R) = (1 - R)^2/2R = \alpha/S \quad (3)$$

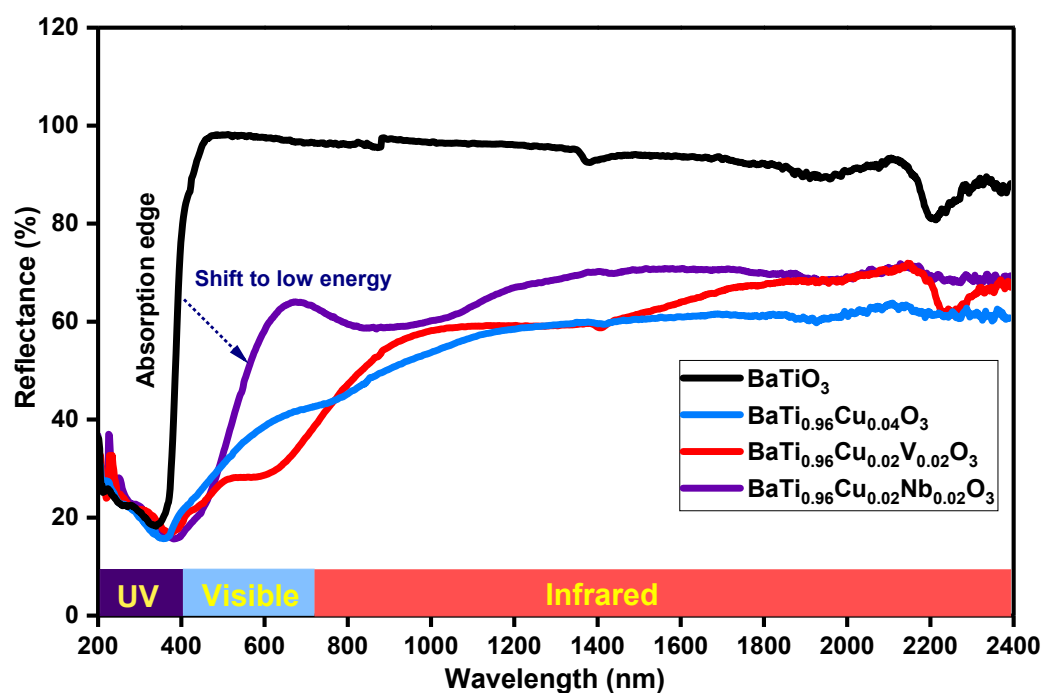


Figure 7. Diffuse reflectance (DR) spectra of BaTiO_3 , $\text{BaTi}_{0.96}\text{Cu}_{0.04}\text{O}_3$, $\text{BaTi}_{0.96}\text{Cu}_{0.02}\text{V}_{0.02}\text{O}_3$ and $\text{BaTi}_{0.96}\text{Cu}_{0.02}\text{Nb}_{0.02}\text{O}_3$ powders.

In both equations, the α represents the absorption coefficient, $h\nu$ is the photon energy, E_g is the band gap energy, $F(R)$ is the Kubelka–Munk function, R is the reflectance and S is the scattering coefficient. As represented in Figure 8, the plot of $[F(R)h\nu]^2$ with $h\nu$ (photon energy) gives the band gap energy of the BaTiO_3 , $\text{BaTi}_{0.96}\text{Cu}_{0.04}\text{O}_3$, $\text{BaTi}_{0.96}\text{Cu}_{0.02}\text{V}_{0.02}\text{O}_3$ and $\text{BaTi}_{0.96}\text{Cu}_{0.02}\text{Nb}_{0.02}\text{O}_3$ samples. The measured value of the energy band gap of the undoped BaTiO_3 catalyst was identified to be 3.2 eV, which is in agreement with the published studies [29,30]. The valence band maximum (VBM) of the BaTiO_3 structure is principally composed of Ti 3d and O 2p states, while the conduction band minimum (CBM) basically consists of Ti 3d states [30]. Owing to the incorporation of Cu, (Cu, V) and (Cu, Nb) ions, the band gap energy of the BaTiO_3 structure was reduced to 2.99 eV

($\lambda = 414$ nm), 2.84 eV ($\lambda = 436$ nm) and 2.72 eV ($\lambda = 455$ nm), respectively. The results of the optical properties prove that the dopants-treated BaTiO₃ catalysts have high visible light absorption compared to the pure one. Owing to the insertion of Cu²⁺, V⁴⁺ and Nb⁵⁺ ions, the conduction band (CB) is possibly derived from Cu-3d, V-3d or Nb-4d and Ti-3d electrons, while the valence band (VB) mostly arises from Cu-3d, V-3d or Nb-4d plus O-2p and Ti-3d states. As a result, the intense reductions of the band gap energy of BaTi_{0.96}Cu_{0.04}O₃, BaTi_{0.96}Cu_{0.02}V_{0.02}O₃ and BaTi_{0.96}Cu_{0.02}Nb_{0.02}O₃ catalysts can be assigned to the presence of impurity states below the conduction band (CB) and above the valence band (VB) due to Cu²⁺, V⁴⁺ and Nb⁵⁺ ions and the formation of oxygen vacancies for charge neutrality [18,30,31]. The sunlight spectrum has nearly 52% infrared red radiation (700–2500 nm), 43% visible light rays (400–700 nm) and 5% ultraviolet wavelengths (280–400 nm) [32]. The optical characteristics prove the suitability of the engineered band gap BaTi_{0.96}Cu_{0.02}V_{0.02}O₃ and BaTi_{0.96}Cu_{0.02}Nb_{0.02}O₃ catalysts for photocatalytic applications under visible light irradiation. In addition, the presence of long absorption states (as illustrated in Figure 8) of BaTi_{0.96}Cu_{0.04}O₃, BaTi_{0.96}Cu_{0.02}V_{0.02}O₃ and BaTi_{0.96}Cu_{0.02}Nb_{0.02}O₃ catalysts support the wide-ranging visible light absorption of the treated samples.

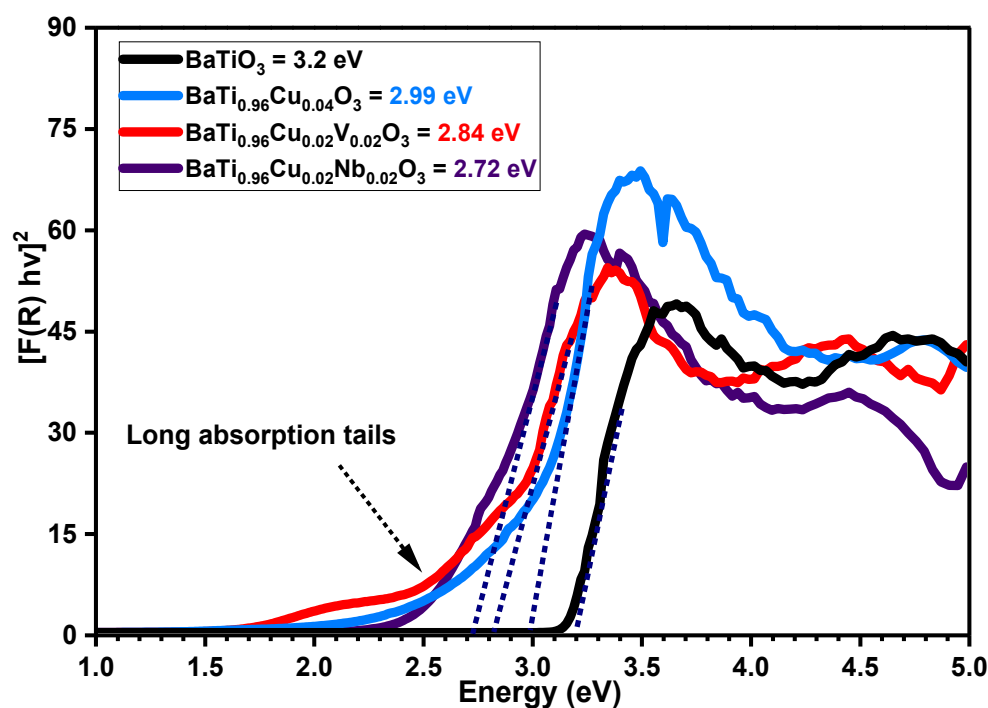


Figure 8. Estimation of band gap energy of BaTiO₃, BaTi_{0.96}Cu_{0.04}O₃, BaTi_{0.96}Cu_{0.02}V_{0.02}O₃ and BaTi_{0.96}Cu_{0.02}Nb_{0.02}O₃ powders.

2.4. Depollution Properties of the Photocatalysts

The photocatalytic depollution properties of BaTiO₃, BaTi_{0.96}Cu_{0.04}O₃, BaTi_{0.96}Cu_{0.02}V_{0.02}O₃ and BaTi_{0.96}Cu_{0.02}Nb_{0.02}O₃ catalysts toward polluted water containing methyl green and methyl orange were studied under natural sunlight and Xenon lamp photoreactor irradiation. Figure 9 shows the change in absorption spectra of methyl green (20 mg/L, catalyst dose 40 mg/100 mL) in the presence of pure BaTiO₃, BaTi_{0.96}Cu_{0.04}O₃, BaTi_{0.96}Cu_{0.02}V_{0.02}O₃ and BaTi_{0.96}Cu_{0.02}Nb_{0.02}O₃ catalysts during 60 min of natural sunlight irradiation. In a sequenced manner, the pure BaTiO₃ catalyst displays low decreases in the absorbance with time with a measured efficiency of 33% during this period. The reductions of the absorbance curve are more noticeable for the BaTi_{0.96}Cu_{0.04}O₃ catalyst, and the photodegradation activity value was estimated to be 67% in the same period. In case of BaTi_{0.96}Cu_{0.02}V_{0.02}O₃ and BaTi_{0.96}Cu_{0.02}Nb_{0.02}O₃ catalysts, the absorbance curve of methyl green dye was powerfully decreased with full degradation activity of 93% and 97%, respectively. The degradation

performance of these catalysts was completely assigned to the photocatalytic process, since the adsorption capacity of all samples was nearly lower than 5% as illustrated in Figure 10. For kinetic study, the rate constant of the photodegradation reactions was estimated using the non-linear least squares analysis according to [1,2]:

$$A = Xe^{-Kt} + E \quad (4)$$

where A represents the polluted molecules calculated residual, X indicates the amplitude of the process, K symbolizes the pseudo-first-order rate constant and E signifies the endpoint. As shown in Figure 11, the measured photodegradation rate constants based on non-linear least squares analysis were 0.0065 ($R^2 = 0.98$), 0.016 ($R^2 = 0.98$), 0.03 ($R^2 = 0.96$) and 0.035 min^{-1} ($R^2 = 0.96$) for BaTiO_3 , $\text{BaTi}_{0.96}\text{Cu}_{0.04}\text{O}_3$, $\text{BaTi}_{0.96}\text{Cu}_{0.02}\text{V}_{0.02}\text{O}_3$ and $\text{BaTi}_{0.96}\text{Cu}_{0.02}\text{Nb}_{0.02}\text{O}_3$ catalysts, respectively.

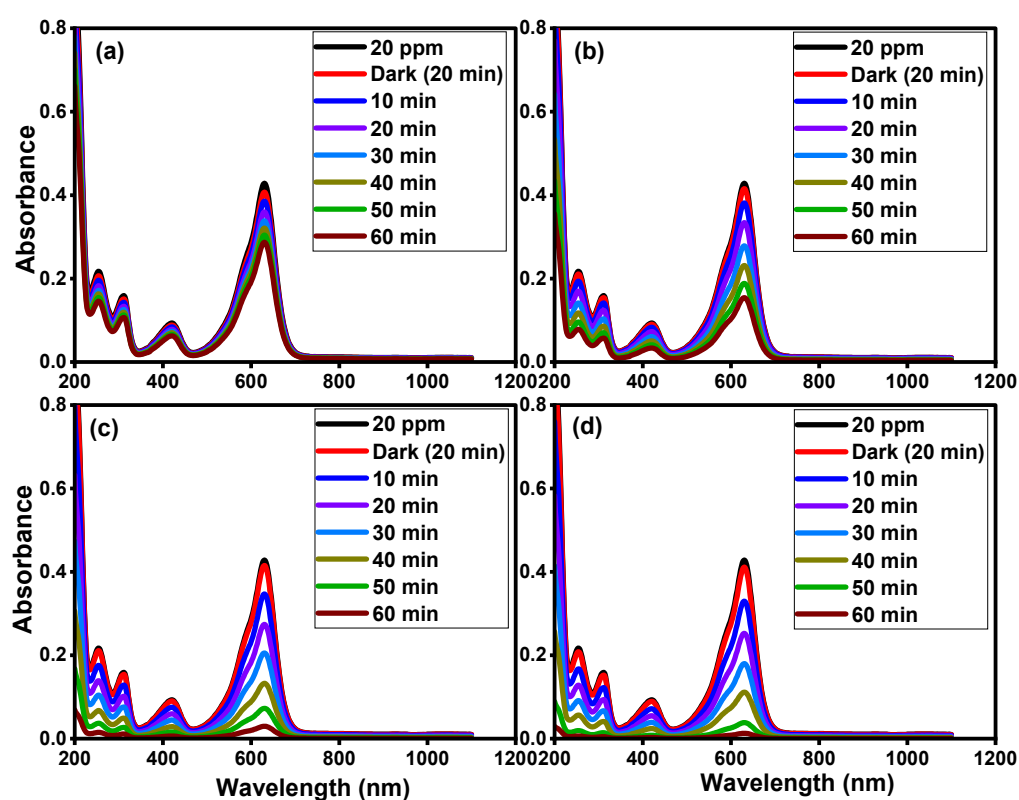


Figure 9. Absorbance curves of 20 ppm methyl green of (a) BaTiO_3 , (b) $\text{BaTi}_{0.96}\text{Cu}_{0.04}\text{O}_3$, (c) $\text{BaTi}_{0.96}\text{Cu}_{0.02}\text{V}_{0.02}\text{O}_3$ and (d) $\text{BaTi}_{0.96}\text{Cu}_{0.02}\text{Nb}_{0.02}\text{O}_3$ powders during sunlight irradiation.

Figure 12a–d show the measurements of the reusability performance, efficient reactive radicals, total organic carbon (TOC) and photodegradation efficiency of methyl green under Xenon lamp irradiation compared to natural sunlight irradiation for $\text{BaTi}_{0.96}\text{Cu}_{0.02}\text{Nb}_{0.02}\text{O}_3$ catalyst, respectively. In the reusability test, as shown in Figure 12a, during three repeated cycles, the $\text{BaTi}_{0.96}\text{Cu}_{0.02}\text{Nb}_{0.02}\text{O}_3$ catalyst revealed high efficiencies of 97, 95 and 94% toward 20 ppm methyl green solution. The high photodegradation activity of the $\text{BaTi}_{0.96}\text{Cu}_{0.02}\text{Nb}_{0.02}\text{O}_3$ catalyst reflects the high stability for multiple uses. To analyze the reactive radicals which have the main effects during the photodegradation reaction, four trapping agents [33] including silver nitrate (AgNO_3), isopropyl alcohol (IPA), triethanolamine (TEOA) and benzoquinone (BQ) were used to capture the electrons (e^-), hydroxyl ($\cdot\text{OH}$) radicals, holes (h^+) and superoxide ($\text{O}_2^{\cdot-}$) species, respectively, as clarified in Figure 12b. The photodegradation activity of the $\text{BaTi}_{0.96}\text{Cu}_{0.02}\text{Nb}_{0.02}\text{O}_3$ catalyst against 20 mg/L methyl green dye was obviously decreased after the addition of TEOA and BQ substances which verifies that the holes (h^+) and superoxide ($\text{O}_2^{\cdot-}$) species are the basic

radicals in the photo-removal process. Figure 12c displays the measurement of the total organic carbon (TOC) analysis of 20 mg/L methyl green dye for $\text{BaTi}_{0.96}\text{Cu}_{0.02}\text{Nb}_{0.02}\text{O}_3$ catalyst under sunlight irradiation. The total organic carbon analysis was carried out to investigate the mineralization behavior of methyl green dye to CO_2 and H_2O through the photocatalysis process. The obtained results prove that the rate of the total organic carbon was decreased with the sunlight irradiation time, reaching a photo-removal value of 94% after 70 min, demonstrating the complete photodegradation of methyl green dye using the $\text{BaTi}_{0.96}\text{Cu}_{0.02}\text{Nb}_{0.02}\text{O}_3$ catalyst to CO_2 and H_2O (simple products). As a result, these findings point out that the $\text{BaTi}_{0.96}\text{Cu}_{0.02}\text{Nb}_{0.02}\text{O}_3$ catalyst has a high mineralization efficiency beside the decolorization reaction. Figure 12d shows the photodegradation activity of the $\text{BaTi}_{0.96}\text{Cu}_{0.02}\text{Nb}_{0.02}\text{O}_3$ catalyst toward 20 mg/L methyl green dye under direct sunlight and Xenon lamp irradiation. Under both irradiation sources, the photodegradation activity of the $\text{BaTi}_{0.96}\text{Cu}_{0.02}\text{Nb}_{0.02}\text{O}_3$ catalyst was 97 and 99%, indicating the robust photocatalytic characteristics under the free solar energy to remove the methyl green dye in 60 min.

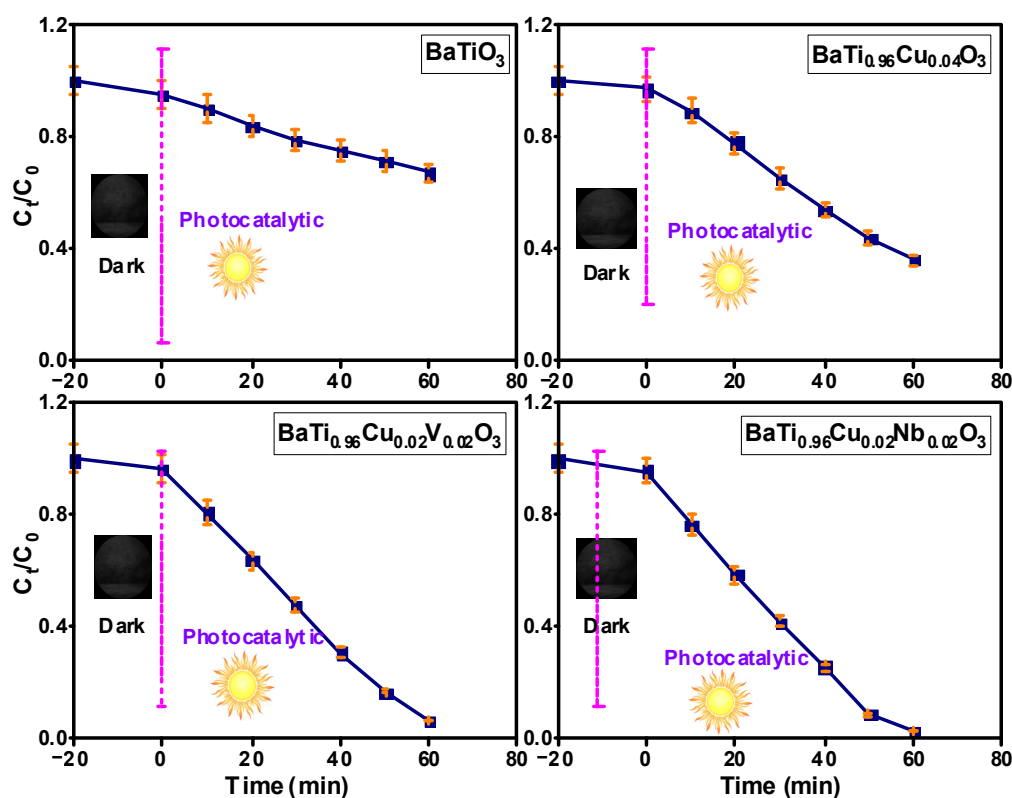


Figure 10. Plots of C_t/C_0 with time (min) of BaTiO_3 , $\text{BaTi}_{0.96}\text{Cu}_{0.04}\text{O}_3$, $\text{BaTi}_{0.96}\text{Cu}_{0.02}\text{V}_{0.02}\text{O}_3$ and $\text{BaTi}_{0.96}\text{Cu}_{0.02}\text{Nb}_{0.02}\text{O}_3$ powders.

The photodegradation of methyl orange pollutant (MO) as an anionic organic dye was investigated using the $\text{BaTi}_{0.96}\text{Cu}_{0.02}\text{Nb}_{0.02}\text{O}_3$ catalyst (best sample) under natural sunlight irradiation. Figure 13 illustrates the change in the absorption spectra of methyl orange dye (concentration = 20 mg/L, catalyst dose = 40 mg/100 mL) in the presence of the $\text{BaTi}_{0.96}\text{Cu}_{0.02}\text{Nb}_{0.02}\text{O}_3$ catalyst during 90 min of sunlight illumination. Gradual and notable decreases of the absorption curve of methyl orange dye with time were seen to reach the final photodegradation efficiency of 94%. As shown in Figure 14a, the plot of C_t/C_0 with time for methyl orange dye degradation decreased with the sunlight irradiation. The kinetic plot of the $\text{BaTi}_{0.96}\text{Cu}_{0.02}\text{Nb}_{0.02}\text{O}_3$ catalyst for methyl orange dye reveals that the rate constant was 0.028 min^{-1} , and the degradation reaction obeys the pseudo-first-order kinetic model with an R-square value of 0.92, as shown in Figure 14b. The stability or the reusability test of the $\text{BaTi}_{0.96}\text{Cu}_{0.02}\text{Nb}_{0.02}\text{O}_3$ catalyst for 20 mg/L of methyl orange dye

during three cycles proves the high photodegradation properties of this composition with final efficiencies of 94, 91 and 88%, as depicted in Figure 14c. The photocatalytic results of both dyes (methyl green and methyl orange) prove the superior photodegradation features of the $\text{BaTi}_{0.96}\text{Cu}_{0.02}\text{Nb}_{0.02}\text{O}_3$ catalyst for practical uses under natural and free sunlight energy.

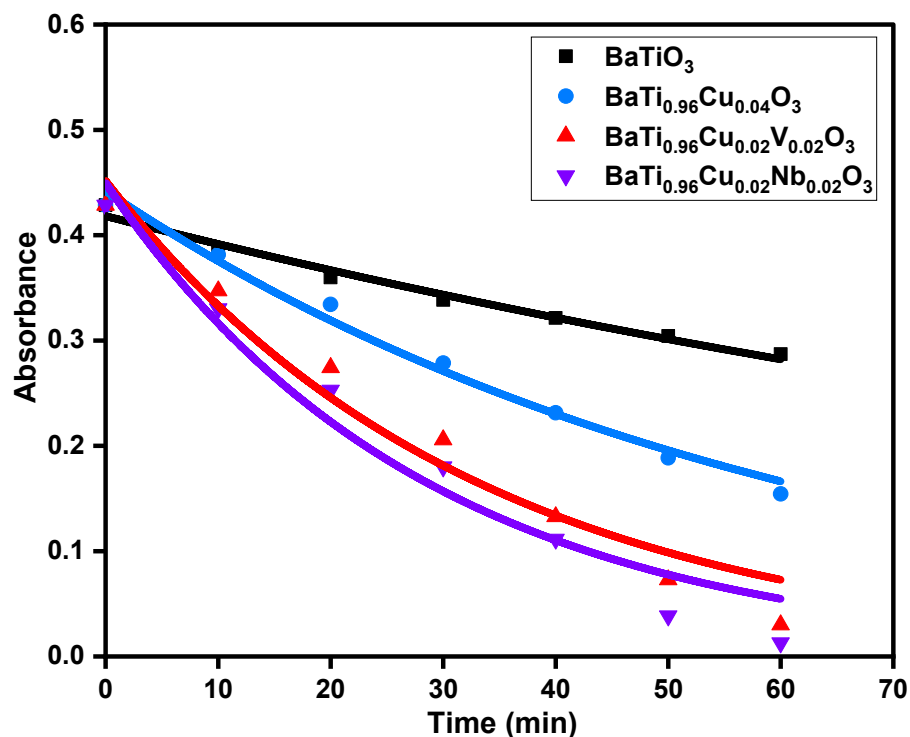


Figure 11. Displays the non-linear first-order fitting of all BaTiO_3 , $\text{BaTi}_{0.96}\text{Cu}_{0.04}\text{O}_3$, $\text{BaTi}_{0.96}\text{Cu}_{0.02}\text{V}_{0.02}\text{O}_3$ and $\text{BaTi}_{0.96}\text{Cu}_{0.02}\text{Nb}_{0.02}\text{O}_3$ samples.

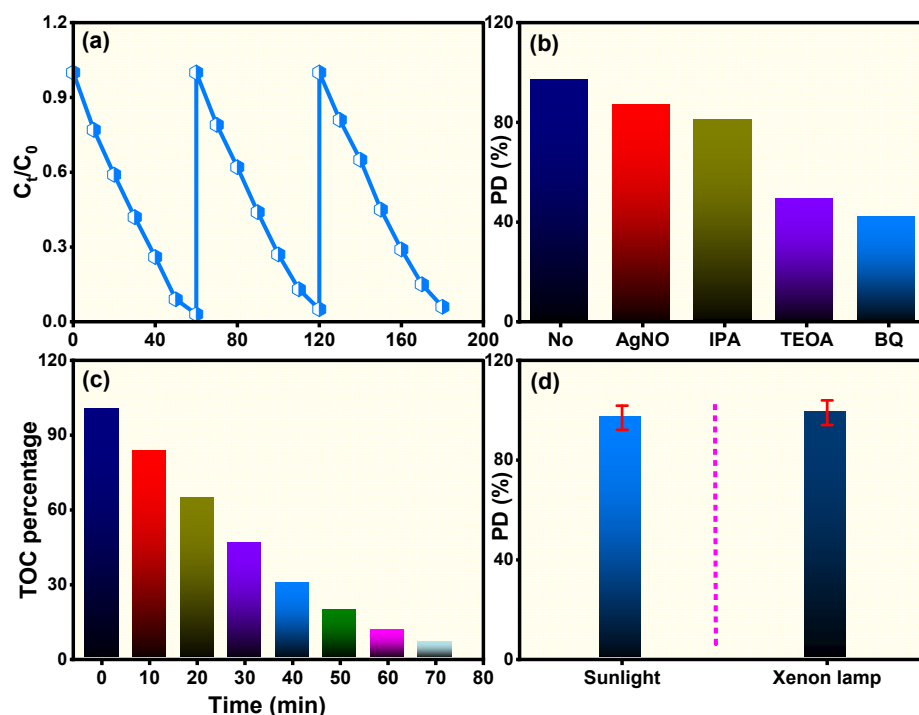


Figure 12. Shows the measurements of (a) reusability, (b) effective radicals, (c) total organic carbon and (d) the photodegradation efficiency under a Xenon lamp compared to sunlight irradiation for the $\text{BaTi}_{0.96}\text{Cu}_{0.02}\text{Nb}_{0.02}\text{O}_3$ catalyst.

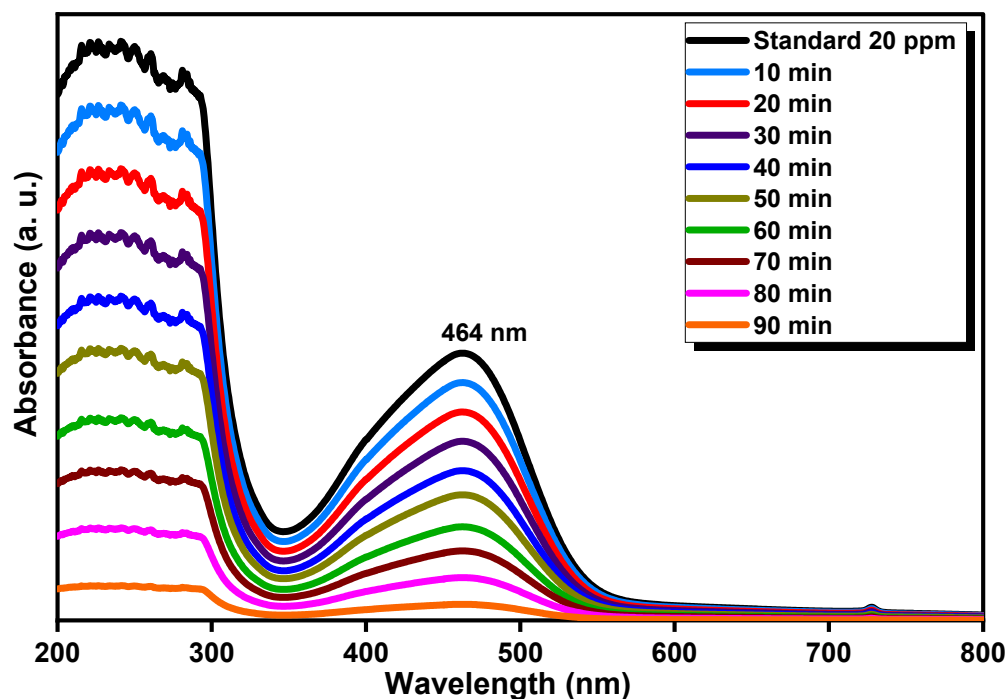


Figure 13. Absorbance curves of 20 mg/L methyl orange of $\text{BaTi}_{0.96}\text{Cu}_{0.02}\text{Nb}_{0.02}\text{O}_3$ powder during natural sunlight irradiation.

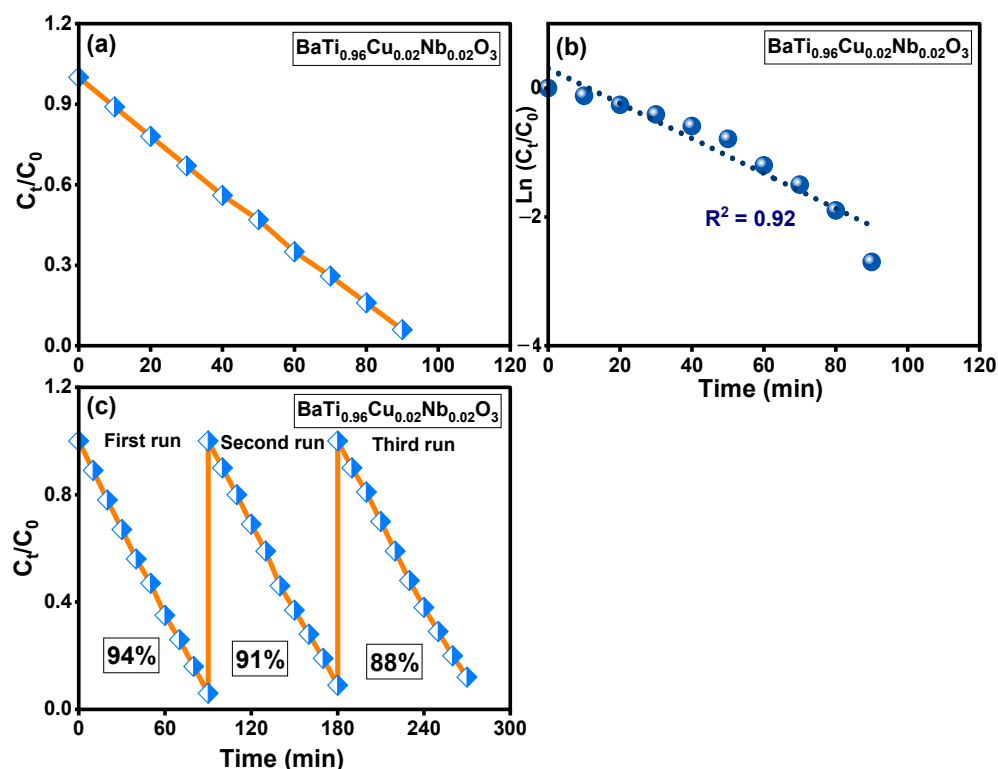
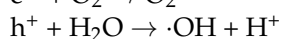
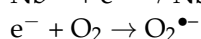
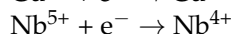
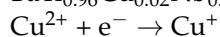
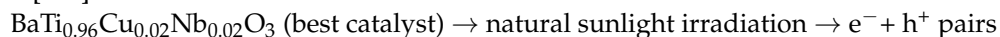


Figure 14. Illustrates (a) plot of C_t/C_0 with time (min), (b) plot of $\ln(C_t/C_0)$ with time (min) and (c) reusability test of 20 mg/L methyl orange for $\text{BaTi}_{0.96}\text{Cu}_{0.02}\text{Nb}_{0.02}\text{O}_3$ catalyst.

The photocatalytic reaction or mechanism for the degradation of the tested organic dyes (methyl green and methyl orange) of the $\text{Bi}_{0.96}\text{La}_{0.02}\text{Gd}_{0.02}\text{FeO}_3$ catalyst essentially depends on the photo-excitation of the electrons from the top of the valence band (VB) to the bottom of the conduction band (CB) by sunlight energy. The photogenerated electrons

in the conduction band (CB) attack the oxygen molecules present in solution to form the superoxide ($O_2^{\bullet-}$) species, whereas the positive holes (h^+) linked to the water molecules to yield the hydroxyl ($\cdot OH$) radicals, respectively. The strong interaction between $\cdot OH$ and $O_2^{\bullet-}$ radicals and methyl green or methyl orange produces CO_2 and H_2O , as shown below [3–5]:



$(\cdot OH, O_2^{\bullet-}) \rightarrow \text{Methyl green and methyl orange} \rightarrow CO_2 \text{ and } H_2O \text{ (non-harmful products)}$

The remarkable photodegradation efficiency of the $BaTi_{0.96}Cu_{0.02}Nb_{0.02}O_3$ catalyst can be related mainly to three factors including the high visible light absorption capacity, homogenous morphology of the grains and the efficient dual dopants separation of the charge carriers (electron–hole pairs).

Figure 15 depicts the X-ray diffraction patterns of the $BaTi_{0.96}Cu_{0.02}Nb_{0.02}O_3$ catalyst before and after the photodegradation test for methyl green dye. The X-ray diffraction peaks of both powders have a good relative intensity and indexed to the tetragonal $BaTiO_3$ structure, confirming the stability of the $BaTi_{0.96}Cu_{0.02}Nb_{0.02}O_3$ catalyst after the photocatalytic degradation reaction. Ahamed et al. [34] reported that Zn-doped $BaTiO_3$ exhibits a visible light photodegradation efficiency of 85% for 20 mg/L methylene blue in 80 min. Bhat et al. [22] showed that Rh-doped $BaTiO_3$ has a photoactivity of 96% for 10 ppm methylene blue in 120 min. The Mn-doped $BaTiO_3$ nanotube as a photocatalyst exhibited improved visible light photocatalytic activity for methylene blue dye during 300 min [23]. Ag-doped $BaTiO_3$ [24] possesses a visible light photodegradation efficiency of 79% for 20 mg/L rhodamine B. Amaechi et al. [25] showed that Fe-doped $BaTiO_3$ has a sunlight photodegradation efficiency of 75% for 20 mg/L methyl orange dye. In our study, the $BaTi_{0.96}Cu_{0.02}Nb_{0.02}O_3$ catalyst exhibited a photodegradation efficiency of 97% and 94% during 60 and 90 min under natural sunlight, respectively. This comparison illustrates the remarkable photocatalytic efficiency of the $BaTi_{0.96}Cu_{0.02}Nb_{0.02}O_3$ catalyst.

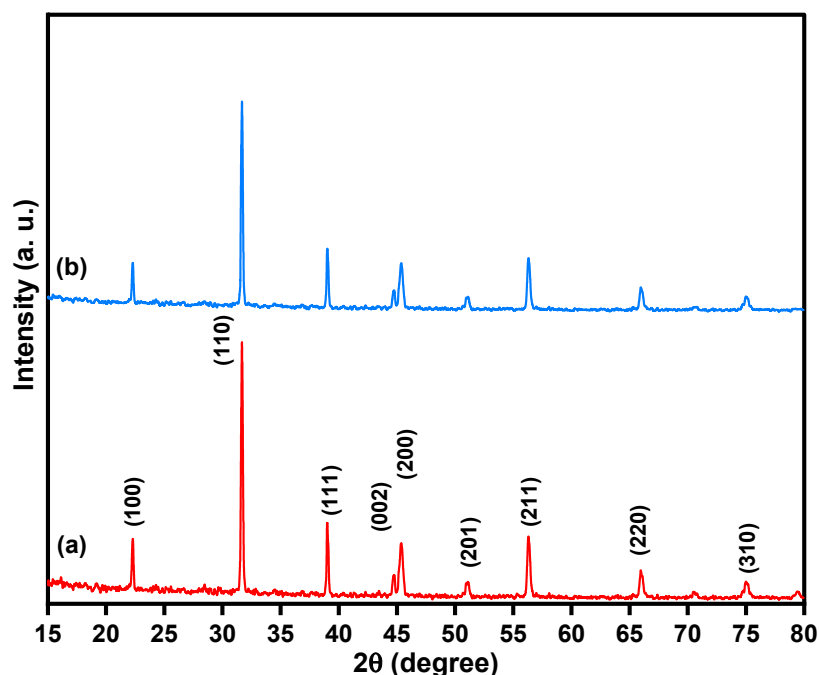


Figure 15. X-ray diffraction patterns of $BaTi_{0.96}Cu_{0.02}Nb_{0.02}O_3$ catalyst (a) before and (b) after the photocatalytic process.

3. Preparation of Samples and Measurements

In this work, all materials were purchased from Sigma-Aldrich (Steinheim, Germany) and used as received. Barium nitrate ($\text{Ba}(\text{NO}_3)_2$, 99.6%), titanium dioxide (TiO_2 , 99.9%), copper(II) nitrate trihydrate ($\text{Cu}(\text{NO}_3)_2 \cdot 3\text{H}_2\text{O}$, 99.95%), ammonium monovanadate (NH_4VO_3 , $\geq 99.0\%$) and niobium(V) chloride (NbCl_5 , 99%) substances were used to prepare the pure BaTiO_3 , $\text{BaTi}_{0.96}\text{Cu}_{0.04}\text{O}_3$, $\text{BaTi}_{0.96}\text{Cu}_{0.02}\text{V}_{0.02}\text{O}_3$ and $\text{BaTi}_{0.96}\text{Cu}_{0.02}\text{Nb}_{0.02}\text{O}_3$ powders by the solid-state reaction method. The used weights for each composition are summarized in Table 2. A pure BaTiO_3 sample was prepared through good mixing of $\text{Ba}(\text{NO}_3)_2$ and TiO_2 (molar ratio 1:1). Then, the obtained mixture was calcined at $600\text{ }^\circ\text{C}$ for 4 h, and after that, the calcination temperature was elevated to $1250\text{ }^\circ\text{C}$ for 5 h and left to cool to room temperature. The $\text{BaTi}_{0.96}\text{Cu}_{0.04}\text{O}_3$, $\text{BaTi}_{0.96}\text{Cu}_{0.02}\text{V}_{0.02}\text{O}_3$ and $\text{BaTi}_{0.96}\text{Cu}_{0.02}\text{Nb}_{0.02}\text{O}_3$ powders were synthesized by the same method through mixing proper weights of the dopants materials (Table 2) with the $\text{Ba}(\text{NO}_3)_2$ - TiO_2 mixture. The X-ray diffraction analysis (PANalytical X-ray diffraction equipment model X'Pert PRO), scanning electron microscope (SEM, model Quanta 250 FEG) and double-beam spectrophotometer JASCO (JASCO, V-570 UV-Vis-NIR) were used to characterize the synthesized BaTiO_3 , $\text{BaTi}_{0.96}\text{Cu}_{0.04}\text{O}_3$, $\text{BaTi}_{0.96}\text{Cu}_{0.02}\text{V}_{0.02}\text{O}_3$ and $\text{BaTi}_{0.96}\text{Cu}_{0.02}\text{Nb}_{0.02}\text{O}_3$ compositions. The photocatalytic properties of pure BaTiO_3 , $\text{BaTi}_{0.96}\text{Cu}_{0.04}\text{O}_3$, $\text{BaTi}_{0.96}\text{Cu}_{0.02}\text{V}_{0.02}\text{O}_3$ and $\text{BaTi}_{0.96}\text{Cu}_{0.02}\text{Nb}_{0.02}\text{O}_3$ powders for the degradation of methyl green and methyl orange dyes were measured using a 100 mL solution of methyl green (20 mg/L) and methyl orange (20 mg/L) plus 40 mg of the catalyst. The effect of adsorption was firstly tested under dark conditions, and then, the mixed solution (catalyst + dye) was exposed to a Xenon lamp or direct sunlight illumination (June, 12–2 pm). Every ten minutes, 4 mL of the exposed solution was taken and centrifuged to eliminate the particles of the powder. The efficiency of the photodegradation process was calculated via measuring the change in absorbance of the maximum peak of methyl green (633 nm) and methyl orange (464 nm). The photodegradation efficiency (PE) is expressed as follows:

$$\text{PE} = A_t/A_0 = C_t/C_0,$$

where A_0 and C_0 signify the primary absorbance and concentration of methyl green and methyl orange, whereas A_t and C_t indicate the absorbance and concentration of methyl green and methyl orange during the different irradiation times.

Table 2. Detailed weights of chemical substances used in the synthesis of BaTiO_3 , $\text{BaTi}_{0.96}\text{Cu}_{0.04}\text{O}_3$, $\text{BaTi}_{0.96}\text{Cu}_{0.02}\text{V}_{0.02}\text{O}_3$ and $\text{BaTi}_{0.96}\text{Cu}_{0.02}\text{Nb}_{0.02}\text{O}_3$ catalysts.

Composition	$\text{Ba}(\text{NO}_3)_2$ (g)	TiO_2 (g)	$\text{Cu}(\text{NO}_3)_2 \cdot 3\text{H}_2\text{O}$ (g)	NH_4VO_3 (g)	NbCl_5 (g)
BaTiO_3	7.84	2.396	-	-	-
$\text{BaTi}_{0.96}\text{Cu}_{0.04}\text{O}_3$	7.84	2.30	0.29	-	-
$\text{BaTi}_{0.96}\text{Cu}_{0.02}\text{V}_{0.02}\text{O}_3$	7.84	2.30	0.1449	0.07	-
$\text{BaTi}_{0.96}\text{Cu}_{0.02}\text{Nb}_{0.02}\text{O}_3$	7.84	2.30	0.1449	-	0.162

4. Conclusions

In this study, a new $\text{BaTi}_{0.96}\text{Cu}_{0.02}\text{Nb}_{0.02}\text{O}_3$ photocatalyst exhibits a high depollution activity for 20 mg/L methyl green and methyl orange pollutants under natural sunlight and Xenon lamp photoreactor irradiations. The solid-state reaction method was used to synthesize high-purity BaTiO_3 , $\text{BaTi}_{0.96}\text{Cu}_{0.04}\text{O}_3$, $\text{BaTi}_{0.96}\text{Cu}_{0.02}\text{V}_{0.02}\text{O}_3$ and $\text{BaTi}_{0.96}\text{Cu}_{0.02}\text{Nb}_{0.02}\text{O}_3$ powders. The X-ray diffraction analysis of all samples proves the formation of a tetragonal perovskite BaTiO_3 structure. The SEM images demonstrate that the addition of the dual dopants of (Cu, V) and (Cu, Nb) ions to BaTiO_3 structure remarkably modifies the morphology of the particles and leads to the formation of uniform semispherical grains. The incorporation of Cu, (Cu, V) and (Cu, Nb) ions adjusts the band gap energy of the BaTiO_3 catalyst to absorb the most visible light spectrum. BaTiO_3 , $\text{BaTi}_{0.96}\text{Cu}_{0.04}\text{O}_3$, $\text{BaTi}_{0.96}\text{Cu}_{0.02}\text{V}_{0.02}\text{O}_3$ and $\text{BaTi}_{0.96}\text{Cu}_{0.02}\text{Nb}_{0.02}\text{O}_3$ powders reveal a band gap energy of

3.2, 2.99, 2.84 and 2.72 eV with the formation of long absorption tails, respectively. The modification of BaTiO₃ by (Cu, Nb) ions induced a superior photodegradation activity for 20 mg/L methyl green and methyl orange pollutants with a total efficiency of 97% and 94% during 60 and 90 min under natural sunlight, respectively. The total organic carbon analysis indicates that the tested dyes were effectively mineralized to CO₂ and H₂O in presence of BaTi_{0.96}Cu_{0.02}Nb_{0.02}O₃ catalyst. In addition, BaTi_{0.96}Cu_{0.02}Nb_{0.02}O₃ catalyst exhibits a high stability for both dyes during three cycles.

Funding: This research received no external funding.

Data Availability Statement: The datasets generated during and/or analyzed during the current study are available from the corresponding author on reasonable request.

Acknowledgments: The authors extend their appreciation to the Deanship of Scientific Research at King Faisal University for the logistic support of this work through Project No. (GRANT 4,195).

Conflicts of Interest: The author declares that they have no known competing financial interests or personal relationships that could have appeared to influence the work reported in this paper.

References

1. Belghiti, M.; Tanji, K.; El Mersly, L.; Lamsayety, I.; Ouzaouit, K.; Faqir, H.; Benzakour, I.; Rafqah, S.; Outzourhit, A. Fast and non-selective photodegradation of basic yellow 28, malachite green, tetracycline, and sulfamethazine using a nanosized ZnO synthesized from zinc ore. *React. Kinet. Mech. Catal.* **2022**, *135*, 2265–2278. [[CrossRef](#)]
2. Dra, A.; Tanji, K.; Arrahli, A.; Iboustaten, E.; El Gaidoumi, A.; Kherchafi, A.; Benabdallah, A.C.; Kherbeche, A. Valorization of Oued Sebou natural sediments (Fez-Morocco Area) as adsorbent of methylene blue dye: Kinetic and thermodynamic study. *Sci. World J.* **2020**, *2020*, 2187129.
3. Abid, M.Z.; Rafiq, K.; Rauf, A.; Shah, S.S.A.; Jin, R.; Hussain, E. Synergism of Co/Na in BiVO₄ microstructures for visible-light driven degradation of toxic dyes in water. *Nanoscale Adv.* **2023**, *5*, 3247–3259. [[CrossRef](#)] [[PubMed](#)]
4. Batra, V.; Kaur, I.; Pathania, D.; Sonu; Chaudhary, V. Efficient dye degradation strategies using green synthesized ZnO-based nanoplateforms: A review. *Appl. Surf. Sci. Adv.* **2022**, *11*, 100314. [[CrossRef](#)]
5. Mzimela, N.; Tichapondwa, S.; Chirwa, E. Visible-light-activated photocatalytic degradation of rhodamine B using WO₃ nanoparticles. *RSC Adv.* **2022**, *12*, 34652–34659. [[CrossRef](#)] [[PubMed](#)]
6. Wu, Y.; Li, Y.; Hu, H.; Zeng, G.; Li, C. Recovering hydrogen energy from photocatalytic treatment of pharmaceutical-contaminated water using Co₃O₄ modified {001}/ $\{101\}$ -TiO₂ nanosheets. *ACS EST Eng.* **2021**, *1*, 603–611. [[CrossRef](#)]
7. Ihsan, A.; Irshad, A.; Warsi, M.F.; Din, M.I.; Zulfqar, S. NiFe₂O₄/ZnO nanoparticles and its composite with flat 2D rGO sheets for efficient degradation of colored and colorless effluents photocatalytically. *Opt. Mater.* **2022**, *134*, 113213. [[CrossRef](#)]
8. Ighnih, H.; Haounati, R.; Malekshah, R.E.; Ouachtak, H.; Jada, A.; Addi, A.A. Photocatalytic degradation of RhB dye using hybrid nanocomposite BiOCl@Kaol under sunlight irradiation. *J. Water Process. Eng.* **2023**, *54*, 103925. [[CrossRef](#)]
9. Pandit, M.A.; Billakanti, S.; Muralidharan, K. A simplistic approach for the synthesis of CuS-CdS heterostructure: A novel photo catalyst for oxidative dye degradation. *J. Environ. Chem. Eng.* **2020**, *8*, 103542. [[CrossRef](#)]
10. Rajan, K.D.; Srinivasan, D.; Gotipamul, P.P.; Khanna, S.; Chidambaram, S.; Rathinam, M. Design of a novel ZnBi₂O₄/Bi₂O₃ type-II photo-catalyst via short term hydrothermal for enhanced degradation of organic pollutants. *Mater. Sci. Eng. B* **2022**, *285*, 115929. [[CrossRef](#)]
11. Darabdhara, J.; Roy, S.; Ahmaruzzaman, M. Efficient photocatalytic degradation of an organic dye by the fabrication of a novel ternary composite based on zeolitic imidazolate framework via a facile in-situ synthetic approach. *Inorg. Chem. Commun.* **2023**, *152*, 110694. [[CrossRef](#)]
12. Beura, R.; Rajendran, S.; Pinilla, M.A.G.; Thangadurai, P. Enhanced photo-induced catalytic activity of Cu ion doped ZnO—Graphene ternary nanocomposite for degrading organic dyes. *J. Water Process. Eng.* **2019**, *32*, 100966. [[CrossRef](#)]
13. Jouali, A.; Salhi, A.; Aguedach, A.; Aarfane, A.; Ghazzaf, H.; Lhadi, E.K.; El krati, M.; Tahiri, S. Photo-catalytic degradation of methylene blue and reactive blue 21 dyes in dynamic mode using TiO₂ particles immobilized on cellulosic fibers. *J. Photochem. Photobiol. A* **2019**, *383*, 112013. [[CrossRef](#)]
14. Borah, D.; Saikia, P.; Sarmah, P.; Gogoi, D.; Rout, J.; Ghosh, N.N.; Bhattacharjee, C.R. Composition controllable alga-mediated green synthesis of covellite CuS nanostructure: An efficient photocatalyst for degradation of toxic dye. *Inorg. Chem. Commun.* **2022**, *142*, 109608. [[CrossRef](#)]
15. Samanta, D.; Basnet, P.; Jha, S.; Chatterjee, S. Proficient route in synthesis of glucose stabilized Ag modified ZnS nanospheres for mechanistic understandings of commercially used dyes degradation. *Inorg. Chem. Commun.* **2022**, *141*, 109498. [[CrossRef](#)]
16. Araujo, R.N.; Nascimento, E.P.; Firmino, H.C.T.; Macedo, D.A.; Neves, G.A.; Morales, M.A.; Menezes, R.R. α -Fe₂O₃ fibers: An efficient photocatalyst for dye degradation under visible light. *J. Alloys Compd.* **2021**, *882*, 160683. [[CrossRef](#)]
17. Ismail, A.A.; Faisal, M.; Al-Haddad, A. Mesoporous WO₃-graphene photocatalyst for photocatalytic degradation of Methylene Blue dye under visible light illumination. *J. Environ. Sci.* **2018**, *66*, 328–337. [[CrossRef](#)]

18. Uma, P.I.; Shenoy, U.S.; Bhat, D.K. Doped BaTiO₃ cuboctahedral nanoparticles: Role of copper in photocatalytic degradation of dyes. *Appl. Surf. Sci. Adv.* **2023**, *15*, 100408. [[CrossRef](#)]
19. Ray, S.K.; Cho, J.; Hur, J. A critical review on strategies for improving efficiency of BaTiO₃-based photocatalysts for wastewater treatment. *J. Environ. Manag.* **2021**, *290*, 112679. [[CrossRef](#)]
20. Masekela, D.; Hintsho-Mbita, N.C.; Sam, S.; Yusuf, T.L.; Mabuba, N. Application of BaTiO₃-based catalysts for piezocatalytic, photocatalytic and piezophotocatalytic degradation of organic pollutants and bacterial disinfection in wastewater: A comprehensive review. *Arab. J. Chem.* **2023**, *16*, 104473. [[CrossRef](#)]
21. Elmahgary, M.G.; Mahran, A.M.; Ganoub, M.; Abdellatif, S.O. Optical investigation and computational modelling of BaTiO₃ for optoelectronic devices applications. *Sci. Rep.* **2023**, *13*, 4761. [[CrossRef](#)] [[PubMed](#)]
22. Bhat, D.K.; Bantawala, H.; Shenoy, U.S. Rhodium doping augments photocatalytic activity of barium titanate: Effect of electronic structure engineering. *Nanoscale Adv.* **2020**, *2*, 5688–5698. [[CrossRef](#)] [[PubMed](#)]
23. Nageri, M.; Kumar, V. Manganese-doped BaTiO₃ nanotube arrays for enhanced visible light photocatalytic applications. *Mater. Chem. Phys.* **2018**, *213*, 400–405. [[CrossRef](#)]
24. Khan, M.A.M.; Kumar, S.; Ahmed, J.; Ahamed, M.; Kumar, A. Influence of silver doping on the structure, optical and photocatalytic properties of Ag-doped BaTiO₃ ceramics. *Mater. Chem. Phys.* **2021**, *259*, 124058. [[CrossRef](#)]
25. Amaechi, I.C.; Youssef, A.H.; Kolhatkar, G.; Rawach, D.; Gomez-Yañez, C.; Claverie, J.P.; Sun, S.; Ruediger, A. Ultrafast microwave-assisted hydrothermal synthesis and photocatalytic behaviour of ferroelectric Fe³⁺-doped BaTiO₃ nanoparticles under simulated sunlight. *Catal. Today* **2021**, *360*, 90–98. [[CrossRef](#)]
26. Kim, J.-H.; Jung, W.-S.; Kim, H.-T.; Yoon, D.-H. Properties of BaTiO₃ synthesized from barium titanate oxalate. *Ceram. Int.* **2009**, *35*, 2337–2342. [[CrossRef](#)]
27. Khan, M.; Mishra, A.; Shukla, J.; Sharma, P. X-ray analysis of BaTiO₃ ceramics by Williamson-Hall and size strain plot methods. *Nanoscale Res. Lett.* **2021**, *16*, 115.
28. Salem, B.B.; Essalah, G.; Ameer, S.B.; Duponchel, B.; Guermazi, H.; Guermazia, S.; Leroy, G. Synthesis and comparative study of the structural and optical properties of binary ZnO-based composites for environmental applications. *RSC Adv.* **2023**, *13*, 6287–6303. [[CrossRef](#)] [[PubMed](#)]
29. Kappadan, S.; Thomas, S.; Kalarikkal, N. Enhanced photocatalytic performance of BaTiO₃/g-C₃N₄ heterojunction for the degradation of organic pollutants. *Chem. Phys. Lett.* **2021**, *771*, 138513. [[CrossRef](#)]
30. Yang, F.; Yang, L.; Ai, C.; Xie, P.; Lin, S.; Wang, C.-Z.; Lu, X. Tailoring bandgap of perovskite BaTiO₃ by transition metals Co-doping for visible-light photoelectrical applications: A first-principles study. *Nanomaterials* **2018**, *8*, 455. [[CrossRef](#)] [[PubMed](#)]
31. Patil, R.P.; Karanjekar, A.N.; Gaikwad, V.B.; Jain, G.H.; Shinde, S.D. Doping-induced diffused phase transition triggers gas-sensing performance of Sn-doped BaTiO₃ nanostructures. *Surf. Interface Anal.* **2022**, *54*, 25–36. [[CrossRef](#)]
32. Morimoto, T.; Oka, R.; Minagawaa, K.; Masui, T. Novel near-infrared reflective black inorganic pigment based on cerium vanadate. *RSC Adv.* **2022**, *12*, 16570–16575. [[CrossRef](#)]
33. Jiang, G.; Wei, Z.; Chen, H.; Du, X.; Li, L.; Liu, Y.; Huang, Q.; Chen, W. Preparation of novel carbon nanofibers with BiOBr and AgBr decoration for the photocatalytic degradation of rhodamine B. *RSC Adv.* **2015**, *5*, 30433–30437. [[CrossRef](#)]
34. Ahamed, M.; Khan, M.A.M. Enhanced photocatalytic and anticancer activity of Zn-doped BaTiO₃ nanoparticles prepared through a green approach using Banana Peel extract. *Catalysts* **2023**, *13*, 985. [[CrossRef](#)]

Disclaimer/Publisher’s Note: The statements, opinions and data contained in all publications are solely those of the individual author(s) and contributor(s) and not of MDPI and/or the editor(s). MDPI and/or the editor(s) disclaim responsibility for any injury to people or property resulting from any ideas, methods, instructions or products referred to in the content.